ION BEAM DYNAMICS

https://doi.org/10.46813/2025-158-071

LONG-RANGE EFFECT UNDER TiO_2 SAMPLES IRRADIATION ON THE LINEAR HELIUM IONS ACCELERATOR

K.V. Pavlii*, V.I. Butenko, O.F. Dyachenko, O.V. Manuilenko, B.V. Zajtsev
National Science Center "Kharkiv Institute of Physics and Technology", Kharkiv, Ukraine
****E-mail: kvint@kipt.kharkov.ua***

The main parameters of sample irradiation on a linear helium ions accelerator and the characteristics of the irradiated TiO_2 samples are presented. After irradiating TiO_2-2 with 4 MeV helium ions, the formation of flaking on the front and back sides of the sample was observed, along with a decrease in bulk electrical resistivity, a decrease in surface electrical resistivity on the front and back sides of the sample, an increase in the percentage of titanium, and a decrease in oxygen on the front and back sides of the irradiated sample, indicating the manifestation of the long-range effect. Considering the change in the surface profile of the irradiated samples, primary processes were calculated, namely: ionization, phonon and vacancy formation, segregation, damage, and sputtering. Analysis of experimental data showed that the model based on the processes of excitation and propagation of elastic waves most physically correctly describes some long-range effects.

PACS: 62.20.Dc; 62.20.Fe

INTRODUCTION

During the irradiation of various materials, the long-range effect was discovered [1, 2], which consists of changes in the properties of irradiated materials at distances greater than the penetration depth of implanted particles in these materials.

The obtained experimental results on the study of the long-range effect are manifested in changes in microhardness, wear resistance, etc. of metals [1 - 5], and in changes in resistivity, Hall constant, etc. of semiconductors [2, 6, 7]. Furthermore, the long-range effect manifests in the anomalously deep propagation of defects induced by ion irradiation [8, 9], in the formation of dislocation structures and changes in the structural-phase state in near-surface layers with depths much greater than the penetration range [10, 11], and in the redistribution (segregation) of main material components and the appearance of the implanted element on both sides of the target [8, 9].

To theoretically describe this effect, the following models were developed: a mathematical model [8, 9], a model based on the excitation of elastic waves [1, 2, 12] due to the primary process of phonon formation, a diffusion model [7], a switching wave model [10], an autowave model [1, 11], and others.

The model based on primary radiation processes of elastic wave excitation most physically accurately describes some long-range effects. According to this model, a high-frequency acoustic wave arises in the irradiated material. This wave either transforms into a shock wave or propagates as an acoustic wave. Propagating through the sample volume, it causes defect rearrangement and emission of secondary waves. The determining factor for these rearrangement processes is the pressure in the shock wave.

Due to the multitude of long-range effects, there is no single mechanism to explain this phenomenon.

The goal of this work is to confirm long-range effects by obtaining experimental results during the irradiation of TiO_2-based samples; calculating primary processes occurring during irradiation, namely: ionization, phonon and vacancy formation, segregation, damage, and sputtering; and analyzing the obtained experimental and calculated data.

1. IRRADIATION PARAMETERS AND SAMPLE CHARACTERISTICS

The NSC KIPT operates a linear helium ions (He+) accelerator [13 - 15]. Table 1 shows the main parameters of the helium ions beam during sample irradiation on the linear accelerator.

Table 1

Irradiation parameters

Parameter	Value
Beam energy, MeV	0.12…4
Pulse duration, μs	500
Pulse current, μA	from 1100 down to 300
Current density, part./cm^2	$(0.44…0.15)\cdot10^{13}$
Repetition rate, imp./s	2…5

Fig. 1 shows the accelerator output with the transport line [16, 17] and irradiation chamber.

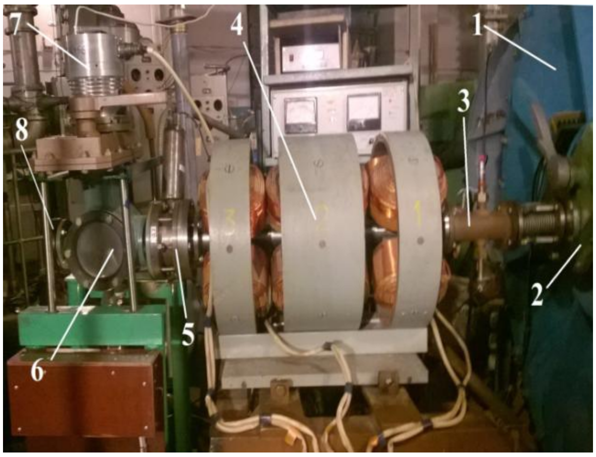

Fig. 1. Output of the linear helium ions accelerator: 1 – accelerator output flange; 2 – valve; 3 – Faraday cup; 4 – focusing triplet; 5 – inductive time-of-flight sensor; 6 – sample irradiation chamber with integrated time-of-flight sensor in front of the sample; 7 – turbo-molecular pump; 8 – window with phosphor

Digital devices connected to a computer for further data recording and processing are used to register irradiation parameters [18].

Works [19 - 23] present experimental techniques and some research results on microscopic, electrophysical, and frictional characteristics of structural materials for Nuclear Power Plants and Thermo-Nuclear Reactors, which were obtained on a linear helium ion accelerator with energies of 0.12 V and 4 MeV.

TiO_2-2 (rutile) samples (diameter = 19.6 mm, thickness = 1.00 mm, ρ = 3.6 g/cm³ = 7.895·10²² atoms/cm³) were selected for irradiation. The elemental composition of the samples (%) is as follows: TiO_2-95.1, Si-2.325, S-0.222, Cl-0.262, Ca-0.067, V-0.895, Fe-0.936, Ni-0.016, Cu-0.055, Zr-0.007, Nb-0.010, Mo-0.009, Pb-0.013, Sn-0.023, I-0.065.

2. EXPERIMENTAL RESULTS

The research methodology for ceramic materials is as follows: after accumulating a certain irradiation dose at 4 MeV energy, microscopic and electrophysical studies of TiO_2-2 samples were carried out. Figs. 2 and 3 show photographs obtained with an electron microscope [22] of the front and back sides of the TiO_2-2 sample, with an irradiation dose of ~$1.2\cdot10^{18}$ ions/cm² and at a temperature of ~60°C. Similar photographs were obtained with an optical microscope at each irradiation dose.

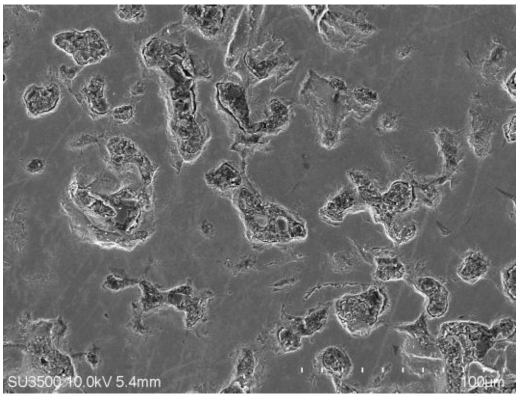

Fig. 2. Topography of TiO_2-2 front surface after irradiation He^+ ions with 4 MeV energy at a temperature of 60°C. Irradiation dose ~$1.2\cdot10^{18}$ ions/cm^2

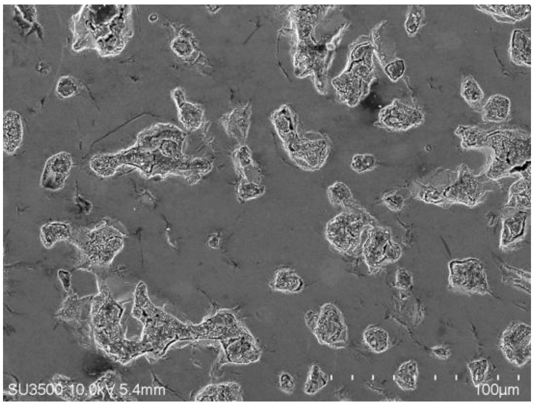

Fig. 3. Topography of TiO_2-2 back surface after irradiation He^+ ions with 4 MeV energy at a temperature of 60°C. Irradiation dose ~$1.2\cdot10^{18}$ ions/cm^2

From the photographs taken with optical and electron microscopes, it follows that the surface is inhomogeneous, has a developed relief, on which traces of the ion beam and craters, and splashes of the sample material are visible. The flaking formation on the front and back sides of the sample is clearly visible. Flaking filling coefficients were calculated: $k = S/S_0$, where S is the area of the sample occupied by flaking, S_0 is the area of the front/back surface of the sample. Fig. 4 shows the dependence of the flaking filling coefficients on the irradiation dose on the front and back surfaces of the sample. The flaking filling coefficients are: k = 0.32 for the front side, k = 0.24 for the back side.

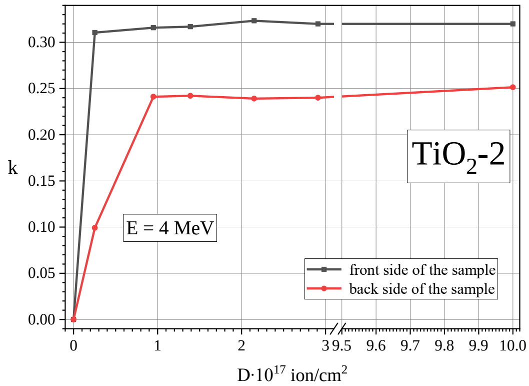

Fig. 4. Dependence of filling coefficients on irradiation dose on the front and back sides of the TiO_2-2 sample

Fig. 5 shows a photo of flaking on the back side of the sample. Similar photos were taken on the front side of TiO_2-2. After processing these photographs, flaking depth distribution profiles were obtained. These dependencies are shown in Figs. 6 and 7.

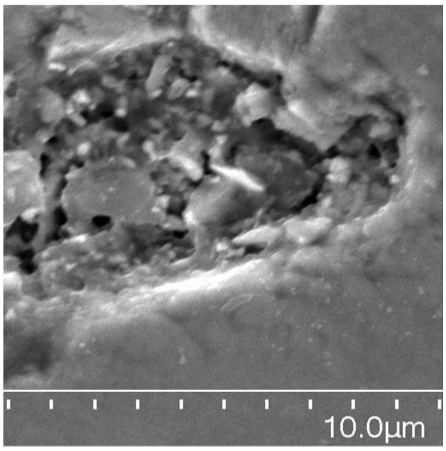

Fig. 5. Flaking on the back side of the sample

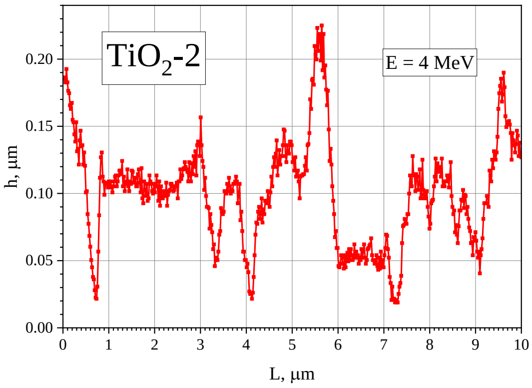

Fig. 6. Flaking depth profile on the back side of the TiO_2-2 sample

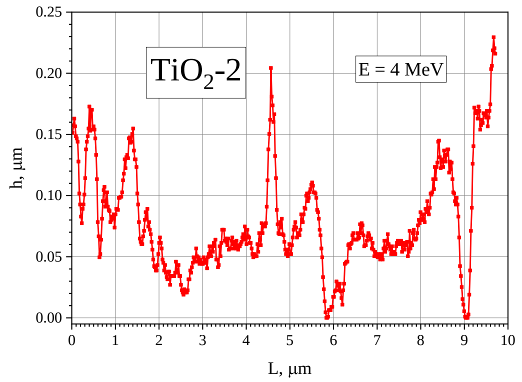

Fig. 7. Flaking depth profile on the front side of the TiO_2-2 sample

From microscopic studies, it follows that with increasing irradiation dose, diffusion channels appear along the perimeter of the formed flaking, as well as directly in the area of flaking formation. The flaking filling coefficient increases up to a dose of ~10^{17} ions/cm², after which it remains practically constant. The average flaking depth, both on the front and back sides of the sample, is ≈ 0.08 µm, and the maximum depths also coincide and are ≈ 0.205 µm. Such a coincidence of geometrical values may indicate a coincidence of the physical mechanisms of flaking formation on the front and back sides of the sample.

After irradiation, X-ray structural studies were performed on the front and back sides of the TiO_2-2 sample. The X-ray structural spectrum of the back side of the irradiated TiO_2-2 sample is shown in Fig. 8.

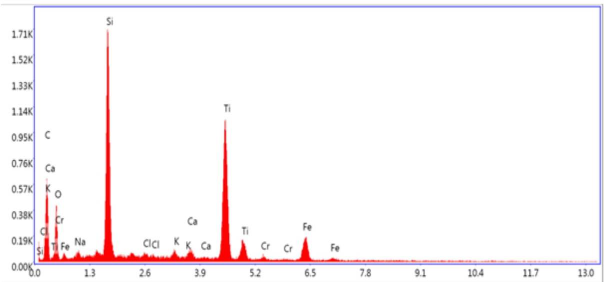

Fig. 8. X-ray structural spectrum of the back side of the irradiated TiO_2-2 sample

Table 2 shows the averaged contents of the main elements (Ti, O) of the initial sample, and the front and back sides of the irradiated sample.

Table 2

Averaged contents of the main elements of the initial sample, front and back sides of irradiated TiO_2-2

Element	Initial sample, %	Front side, %	Back side, %
Ti	31.7	~ 39	~ 34
O	63.4	~ 60	~ 58

It should be noted that there is an increase in the percentage of titanium and a decrease in oxygen on both the front and back sides of the TiO_2-2 sample. This change can only be explained by the dissociation of TiO_2 with subsequent diffusion of oxygen to the sample surface and its partial escape from the sample. In addition, a small segregation of sample elements to its surfaces is observed.

After irradiating the samples with helium ions to a certain dose, the bulk and surface electrical resistivity of the front and back sides of the samples were measured. Fig. 9 shows the dependence of the change in bulk electrical resistivity on the irradiation dose for TiO_2-2, and Fig. 10 shows the dependencies of the surface electrical resistivity of the front and back sides of the sample on the irradiation dose.

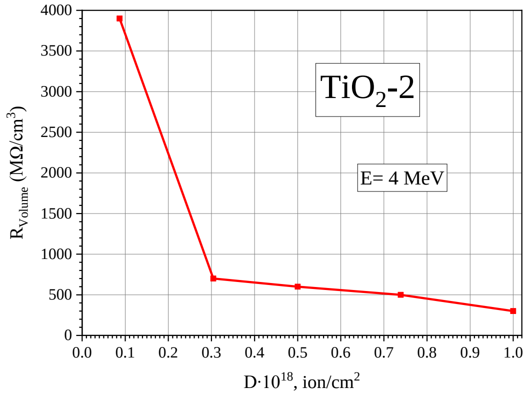

Fig. 9. Change in bulk electrical resistivity with irradiation dose

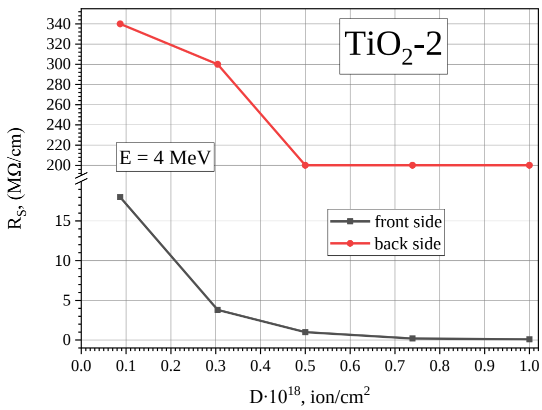

Fig. 10. Change in surface electrical resistivity with irradiation dose on the front and back sides of the sample

From the presented results, it follows that the bulk electrical resistivity decreases up to a dose of ~$1{\cdot}10^{18}$ ions/cm². The surface electrical resistivity of the TiO_2-2 sample on both the front and back sides decreases up to a dose of ~ $0.5{\cdot}10^{18}$ ions/cm². Such changes can only occur due to the dissociation of TiO_2 and the segregation of TiO_2-2 elements throughout the sample volume. It should be noted that after each irradiation session, the samples were kept in air for 24…48 h. After this, the surface and bulk electrical resistivities were measured. A partial recovery of electrical resistivity of no more than 5% was recorded.

3. CALCULATED CHARACTERISTICS

Primary processes occurring during irradiation play a paramount role in changing the physical characteristics of irradiated samples, namely: ionization, phonon and vacancy formation, segregation, and sputtering. The SRIM software package [24, 25] was used to calculate these characteristics. SRIM calculations were performed considering the displacement cascade.

During irradiation of TiO_2-2 on a linear accelerator with 4 MeV helium ions, the surface changes due to flaking formation, and also as a result of sputtering of sample structure atoms. These processes change the surface roughness. As the sample accumulates dose, the depth of hollows on the sample surface increases, and the sputtering efficiency increases because each surface atom is bound to the surface by a smaller number of electrons. Therefore, after irradiation of TiO_2-2, microsurface images were taken. Fig. 11 shows the surface structure of the irradiated TiO_2-2 sample.

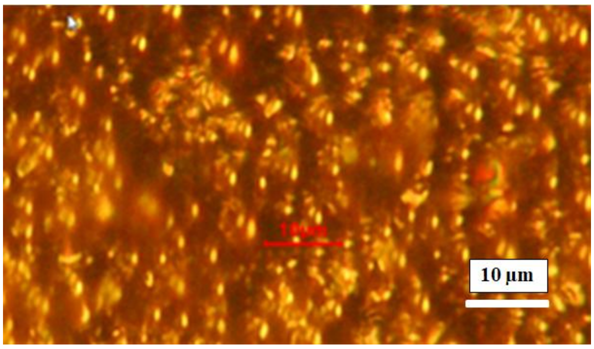

Fig. 11. Surface structure of TiO_2-2, irradiation dose ≈ $1.2 \cdot 10^{18}$ ions/cm²

After processing the microsurface images of the irradiated sample, the change of roughness along the TiO_2-2 surface was obtained, Fig. 12.

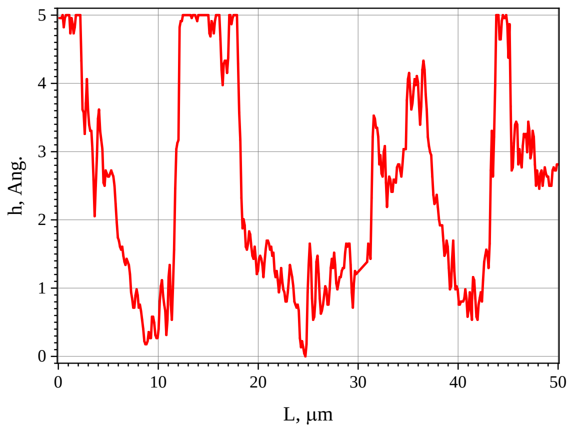

Fig. 12. Change of the roughness of the irradiated TiO_2-2 sample along its surface length, irradiation dose ≈ $1.2 \cdot 10^{18}$ ions/cm²

From Fig. 12, it follows that the front surface of TiO_2-2 is inhomogeneous, has a developed relief, and a maximum hollows depth is no more than 5 Å.

With a change in the surface relief of the samples during irradiation, the angle of incidence of helium ions into the sample changes, and the primary processes and sputtering coefficients of the elements change. In SRIM calculations, these facts were taken into account by changing the angle of incidence of ions into the irradiated samples and a maximum hollows depth.

Table 3 shows the energy losses for ionization, phonon formation, and damage by the helium ion beam and displacement cascades for 4 MeV irradiation energy. The absolute energy values of these processes are also given in the same Table.

Table 3

Calculated characteristics of TiO_2-2

Energy, MeV	Energy loss, %		
	Ionization, He^+/cascade	Phonons, He^+/cascade	Damage, He^+/cascade
4	99.69/0.06	0.04/0.20	0.00/0.01
Energies absolute values, keV/ion			
4	3990.0	1.5/8	0.50

As follows from Table 3, most of the beam energy goes to ionization. Helium ions make the main contribution to ionization. The main contribution to phonon formation and damage comes from displacement cascades. At 4 MeV beam energy, 20 times more energy is spent on phonon formation than on damage. Therefore, the role of phonons and ionization in some radiation effects can be decisive. Fig. 13 shows, in relative units, the profiles of ionization, phonon and vacancy formation, segregation in TiO_2-2 at a helium beam energy of 4 MeV with a uniform distribution of the angle of incidence of helium ions into the sample.

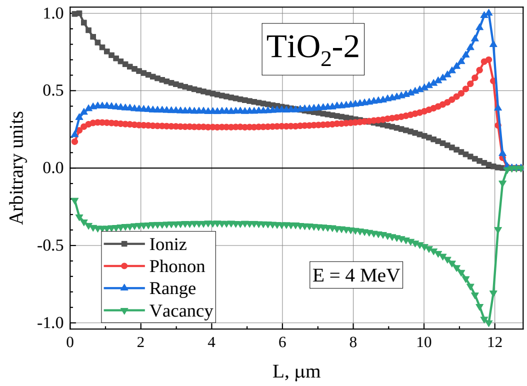

Fig. 13. Profiles of ionization, phonon and vacancy formation, segregation in TiO_2-2

From the graphs in Fig. 13, it follows that in the irradiated TiO_2-2 samples, segregation of material atoms occurs along the path of helium ions. Since segregating atoms play a primary role in changing the thermophysical and electrophysical characteristics of ceramic materials, Table 4 presents the ratios of the main redistributed TiO_2-2 atoms to helium atoms. From these data, the number of segregating atoms is calculated depending on the irradiation dose.

Table 4

Relations of TiO_2-2 redistributed atoms to helium atoms

E = 4 MeV				
O/He	Ti/He	Si/He	S/He	Cl/He
99.90	69.13	2.67	0.152	0.181
Ca/He	V/He	Fe/He	Cu/He	
0.048	0.614	0.661	0.039	

Phonon formation occurs in regions of ionization, segregation, and vacancy formation. A high degree of sample ionization occurs in regions with less phonon, vacancy, and segregation formation. As noted above, displacement cascades make the main contribution to phonon formation. Fig. 14 shows the initial fragment (0…40 Å) of phonon formation profiles due to helium ions and displacement cascades.

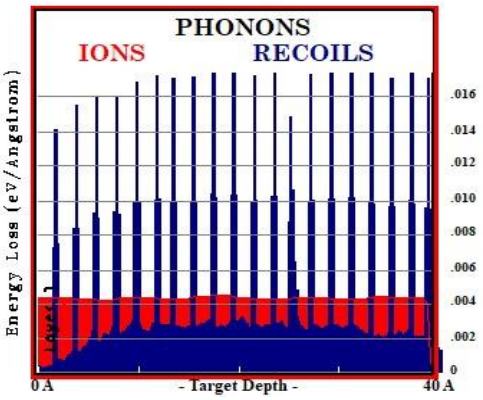

Fig. 14. Fragment of phonon formation profiles due to helium ions (red curve) and displacement cascades (blue curve)

As appears from Fig. 14, displacement cascades create the high-frequency component with the big amplitude of phonons formation (shock waves), and helium ions create the low-frequency component.

TiO_2-2 sputtering coefficients also are calculated with a uniform distribution of the angle of incidence (0…90)°and a maximum hollows depth of 5 Å. TiO_2-2 sputtering coefficients values are resulted in Table 5.

Table 5

TiO_2-2 total sputtering coefficients at E = 4 MeV, the hollows depth = 5 Å

k·10^{-5} atom/ion, E = 4 MeV								
α°	0	6	12	18	24	30	36	42
k	82.7	82.9	82.0	98.2	99.7	98.2	97.2	95.1
α°	48	54	60	66	72	78	84	89
k	92.7	103	102	111	137	165	255	1183

Fig. 15 shows the dependence of the change in the total sputtering coefficient on the angle of incidence of the helium ion beam, considering a maximum hollows depth of 5 Å and He+ range of 100 Å.

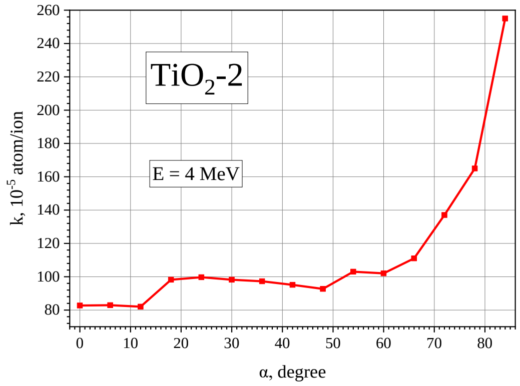

Fig. 15. Dependence of the total sputtering coefficient on the angle of incidence of the helium beam into the TiO_2-2 sample. Angle of incidence range = (0…90)°, He+ path = 100 Å, maximum hollows depth = 5 Å

The range of changes in the sputtering coefficient at α = (0…90)° was: k = (83…1183)·10^{-5} atom/ion. The average values of the total sputtering coefficient, excluding extreme values (i.e., at α = 0° and α = 90°), are: k = 114·10^{-5} atom/ion. Averaging the sputtering coefficient over the hollows depth, we get for E = 4 MeV, k = 57·10^{-5} atom/ion. We believe this is the maximum possible sputtering coefficient for 4 MeV helium ions.

Vacancy formation and the number of displacements per ion in TiO_2-2 samples play a major role in damage calculations (dpa – displacements per atom). The following expression [24] was used to calculate the dpa damage:

$$dpa = \frac{D_{ion} \cdot dpi}{N_A \rho_0 SL} \cdot \frac{1}{100} \sum_i \mu_i n_i ,$$

where D_{ion} is the radiation dose (ion/cm^2, an experimental parameter), dpi is the number of displacements per ion (from SRIM calculations), N_A is Avogadro's number, $m_{mole} = \frac{m}{M}$, $m = \rho_0 \cdot SL$, where ρ_0 is the measured sample density, S = 1 cm^2 is the unit sample area, L is the maximum ions range in the sample, $M = \frac{1}{100} \sum_i \mu_i n_i$ is the sample molar mass, μ_i is the molecular mass of the sample *i-th* element, n_i is the percentage of the sample *i-th* element.

The calculated damage (dpa) for E = 4 MeV was ≈ 5.0 displacements/atom at an irradiation dose of 1·10^{18} ions/cm². The damage profile (dpa) in TiO_2-2 is shown in Fig. 16 and corresponds to an inverted vacancy formation profile (see Fig. 13).

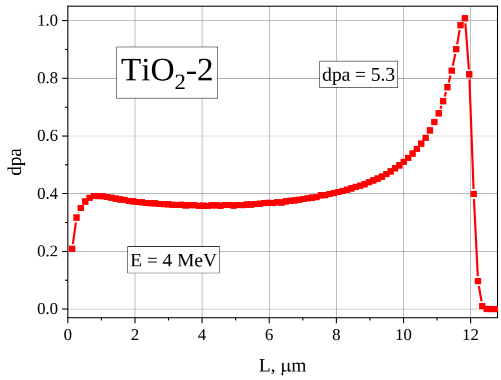

Fig. 16. Damage profile (dpa) in TiO_2-2 sample

4. ANALYSIS AND DISCUSSION OF THE OBTAINED RESULTS

The experimental detection of the long-range effect during the irradiation of TiO_2-2 samples with 4 MeV helium ions consists of the following:

1. Formation of flaking on the front and back sides of the irradiated sample. The flaking areas on the front and back sides of the sample increase with increasing irradiation dose up to 32 and 24%, respectively, and remain practically constant at a dose above ≈ 1·10^{17} ions/cm². The flaking depth on both sides is ≈ 0.08 µm, and the maximum depths also coincide and are ≈ 0.2 µm (see Figs. 4 - 7).

2. Increase in titanium percentage and decrease in oxygen on the front and back sides of the irradiated TiO_2-2 sample (see Table 2).

3. Decrease in surface electrical resistivity on the front and back sides of the sample and decrease in bulk electrical resistivity with increasing irradiation dose. The decrease in bulk electrical resistivity occurs up to a dose of ~1·10^{18} ions/cm². The decrease in surface electrical resistivity on both the front and back sides of the

TiO_2-2 sample occurs up to a dose of ~0.5·10^{18} ions/cm² (see Figs. 9, 10).

The long-range effect can be explained by the complex effect of primary processes (section 3) on the change in the structure of the irradiated TiO_2-2 sample. Sputtering of structure atoms affects only the front side of the sample due to changes in surface relief. This leads to changes in primary processes in the helium ion penetration region, and consequently, to changes in ‘secondary’ processes such as diffusion, re-segregation, and phonon formation, pore growth, grain growth, etc.

The change in sample density along the helium ion path changes the velocities of shock and acoustic waves and is determined by sputtering, segregation, and vacancy formation. The linear coefficients of density change due to sputtering (1), segregation (2), and vacancy formation (3) are determined by:

$$k_{sp}(x) = -\frac{k_{Sum\_sp}}{\sqrt{2\pi}\omega_{sp}x}\exp\left(\frac{-\ln\left(\frac{x}{x_c}\right)^2}{2\omega_{sp}^2}\right), \quad (1)$$

$$k_{seg}(x) = \frac{2\cdot k_{Sum\_seg}}{\pi}\left(\frac{\omega_{seg}}{4\cdot((x-x_c)^2+\omega_{seg}^2)+\omega_{seg}^2}\right), \quad (2)$$

$$k_{vac}(x) = -\frac{2\cdot k_{Sum\_vac}}{\pi}\left(\frac{\omega_{vac}}{4\cdot((x-x_c)^2+\omega_{vac}^2)+\omega_{vac}^2}\right), \quad (3)$$

where k_{Sum_sp}, k_{Sum_seg}, k_{Sum_vac} are the total sputtering coefficients, segregation and vacancy formation (calculated in SRIM program [atom/ion]), ω_{sp}, ω_{seg}, ω_{vac} are logarithmic standard deviations, x_c are the central points, respectively. Table 6 presents the above-mentioned values for TiO_2-2 samples irradiated on a linear helium ion accelerator with energy of 4 MeV.

Table 6

Parameters for (1), (2), (3)

Sputtering		
k_{Sum_sp}	ω_{sp}, [nm]	x_c, [nm]
$98\cdot10^{-5}$	0.818	0.88
Segregation		
k_{Sum_seg}	ω_{seg}, [nm]	x_c, [nm]
181	496.13	11886
Vacancies		
k_{Sum_vac}	ω_{vac}, [nm]	x_c, [nm]
181	482.06	11893

Fig. 17 shows the dependence of the change in the linear density coefficient on the helium ion range at E = 4 MeV.

The first minimum on the graph is formed due to the sputtering of sample structure atoms. The first maximum and the second minimum on the graph are the difference between segregation and vacancy formation processes, formed due to backscattering of structure atoms. Then the change in the density of the irradiated sample can be described by the following expression:

$$\rho(t,\vec{r}) = \rho_0 + \frac{n(t)}{S_0}(k_{sp}(\vec{r}) + k_{seg}(\vec{r}) + k_{vac}(\vec{r})), \quad (4)$$

where ρ_0 is the initial sample density, $n(t)$ is the number of ions per sample area S_0 (i.e. irradiation dose).

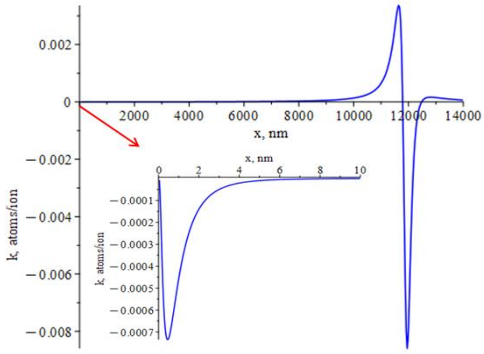

Fig. 17. Change in linear density coefficient along the helium ion range

Phonon formation occurs in regions of ionization, segregation, and vacancy formation (see Fig. 13). As follows from Fig. 14, in the region of helium ion range, a high-frequency shock wave is formed by displacement atoms, and a low-frequency one is formed by helium ions appearing in their passage region. Wave propagation occurs both towards the front surface of the sample and towards its back side, with a change in sample density.

The acoustic wave formed by helium ions can be described by the following expression:

$$u_{Ac}(0,x) = \frac{2S_{Ac}}{\pi}\cdot\frac{w_{Ac}}{4(x-x_c)^2+w_{Ac}^2}, \quad (5)$$

where S_{Ac} is the area under the curve (5), x_c is the center of the curve, $w = FWHM$ is the full width at half maximum. The parameters for expression (5) are as follows: S_{Ac} = 1600 eV, w_{Ac} = 547.86 nm, x_c = 11903 nm.

A single shock wave (see Fig. 14) can be described by a Gaussian distribution:

$$y_i = y_{\max(i)}\cdot\exp\left(-\frac{(x-x_{c(i)})^2}{2\cdot w_{Sh}^2}\right), \quad (6)$$

or a step function:

$$y_i = \begin{cases} y_{\max(i)},\ x_{c(i)} - \frac{2w_{Sh}}{\sqrt{\ln 4}} < x < x_{c(i)} + \frac{2w_{Sh}}{\sqrt{\ln 4}} \\ 0,\ x_{c(i)} + \frac{2w_{Sh}}{\sqrt{\ln 4}} < x < x_{c(i)} - \frac{2w_{Sh}}{\sqrt{\ln 4}} \end{cases}, \quad (7)$$

where $y_{\max}$ is the amplitude, $x_{c(i)}$ is the center of shock wave formation, w_{Sh} = 0.15 nm is the standard deviation. Fig. 18 shows functions (6) and (7).

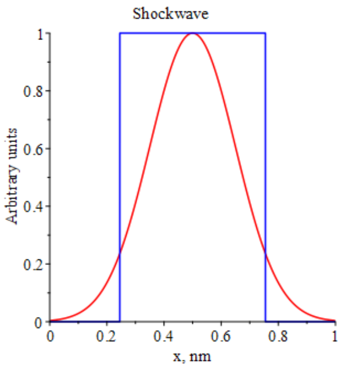

Fig. 18. View of a single shock wave (red – Gaussian distribution, blue – step function)

In (6) and (7) $x_{c(i)}$ takes discrete values and is determined from the expression:

$$x_{c(i)} = x_{c(i-1)} + \Delta, \qquad (\Delta = b_0 + b_1 P + b_2 P^2), \qquad (8)$$

where P is the porosity of the irradiated material in %, b_0= 0.2225 nm, b_1= –8.13·10^{-5} nm, b_2= 4.225·10^{-5} nm.

The shock wave amplitudes ($y_{\max(i)}$) for 4 MeV helium ions energy are determined from the following expression:

$$y_{\max} = \frac{2A}{\pi} \cdot \frac{w}{4(x - x_c)^2 + w^2}, \qquad (9)$$

where A = 8000 eV, x_c = 11885 nm, w = 503,9 nm. It should be noted that x_c corresponds to the TiO_2 lattice distance, and the peak width corresponds to the average atomic diameter of titanium and oxygen. Expressions (1)-(3) and (5)-(9) are obtained by interpolation from calculations in the SRIM program.

Therefore, the formation of shock waves can be described by the following expressions:

$$u_{Sh}(0, x) = \sum_{i=1}^{dpi+i_n} y_{\max(i)} \cdot \exp\left(-\frac{(x - x_{c(i)})^2}{2 \cdot w_{sh}^2} \right), \qquad (10)$$

or:

$$u_{Sh}(0, x) = \sum_{i=1}^{dpi+i_n} \begin{cases} y_{\max(i)}, \; x_{c(i)} - \frac{2w_{Sh}}{\sqrt{\ln 4}} < x < x_{c(i)} + \frac{2w_{Sh}}{\sqrt{\ln 4}} \\ 0, \; x_{c(i)} + \frac{2w_{Sh}}{\sqrt{\ln 4}} < x < x_{c(i)} - \frac{2w_{Sh}}{\sqrt{\ln 4}} \end{cases}. \qquad (11)$$

The value of the coefficient (i_n) in expressions (10), (11) is determined by normalizing these expressions to the energy value of shock wave formation. For TiO_2-2, at a helium ion energy of 4 MeV, E_{Sh} = 8 keV/ion (see Table 3). Since during irradiation of TiO_2-2, ≈ 185 displacements per ion (dpi) are formed, assuming that 1 dpi forms one shock wave, we get that the energy transferred by one shock wave is 43.2 eV. This energy is sufficient for TiO_2 dissociation, as the TiO_2 bond energy is ~ 17 eV. The process of propagation of the formed acoustic and shock waves is described by wave equations with initial formation conditions (5), (10) or (11), considering the change in sample density (4) along the helium ion path.

The main degree of ionization occurs in the region of phonon formation, segregation, and vacancy formation (see Fig. 13). Since the samples are grounded during irradiation and the mobility of electrons is more than 7000 times greater than the mobility of helium ions, the ionization region will be positively charged. Under the influence of the Coulomb field, polarization of structure atoms and segregation occur with their subsequent acceleration and the formation of acoustic and shock waves. These processes occur cyclically throughout the entire volume of the sample. Thus, the beam energy is transferred throughout the entire sample volume, including the front and back sides. The transferred energy is sufficient for TiO_2 dissociation (decrease in electrical resistivity) and the formation of stresses on the front and back sides of the TiO_2-2 sample (flaking formation). In addition, the diffusion of oxygen and helium plays a significant role in flaking formation, which primarily occurs through channels formed along the perimeter of the flaking, as well as directly in the area of its formation (see Fig. 5).

CONCLUSIONS

1. The long-range effect has been confirmed by obtaining experimental results on the formation of flaking on the front and back sides of the sample, changes in the percentage of titanium and oxygen in the irradiated TiO_2-2 samples, and a decrease in bulk and surface electrical resistivity.

2. Primary processes during irradiation of TiO_2-based samples have been calculated, namely: ionization, phonon formation, segregation, vacancy formation, damage, and sputtering coefficients.

3. Analysis of experimental results and calculated data shows the decisive role of phonon formation and sample element ionization processes in explaining the long-range effect.

The model based on primary radiation processes of elastic wave excitation and propagation most physically correctly describes the experimental results obtained during TiO_2-2 irradiation on a linear helium ion accelerator with 4 MeV energy.

REFERENCES

1. N.P. Aparina, M.I. Guseva, B.N. Kolbasov, et al. Some aspects of the long-range effect // *Problems of Atomic Science and Technology*. 2007, № 3, p. 18-27.
2. D.I. Tetelbaum, V.Ya. Bayankin. Long-range effects // *Priroda*. 2005, № 4, p. 9-17.
3. D.I. Tetelbaum, E.V. Kuril'chik, N.D. Latisheva. Long-range effect at low-dose ion and electron irradiation of metals // *Nucl. Instrum. and Meth. in Phys. Res.* 1997, B127/128, p. 153-156.
4. D.I. Tetelbaum, A.Yu. Azov, E.V. Kuril'chik, et al. The long-range influence of the ion and proton irradiation on the mechanical properties and on the composition of the permaloy-79 // *Vacuum*. 2003, v. 70, № 2-3, p. 169-173.
5. D.I. Tetelbaum, E.V. Kuril'chik, Ya.A. Mendeleva. Long-range effect at low-intensity irradiation of solids // *Poverkhnost*. 2009, № 3, p. 1-11 (in Russian).
6. N.P. Morozov, D.I. Tetelbaum. Deep penetration of radiating defects from ion-implanted layer in semiconductor bulk // *Fizika i tekhnika poluprovodnikov*. 1983, v. 17, iss. 5, p. 838-842 (in Russian).
7. N.P. Morozov, V.D. Skupov, D.I. Tetelbaum. Defect formation in silicon during ion bombardment beyond the ion range // *Fizika i tekhnika poluprovodnikov*. 1985, v. 19, iss. 3, p. 464-468 (in Russian).
8. Yu.P. Sharkeev, A.N. Didenko, E.V. Kozlov. High dislocation density structures and hardening produced by high fluency pulsed into beam implantation // *Surface and Coating Technology*. 1994, v. 65, p. 112-120.
9. Yu.P. Sharkeev, E.V. Kozlov, A.N. Didenko, et al. The mechanisms of the long-range effect in metals and alloys by ion implantation // *Surface and Coating Technology*. 1996, v. 83, p. 15-21.
10. Yu.V. Martynenko, P.G. Moskovin. Long-range effect and energy transfer in solids during ion bom-

bardment // *Pis'ma v Zhurnal tekhnicheskoi fiziki*. 1996, v. 22, iss. 17. p. 54-58 (in Russian).
11. C.A. Krivelevich. Switching waves and long-range effects // *Vestn. Nizhegorod. un-ta. Fizika tverdogo tela.* 1998, iss. 2, p. 71-78 (in Russian).
12. F. Mirzoev. Propagation of nonlinear longitudinal waves in a solid with consideration of interaction of deformation fields and defects concentration // *Zhurnal tekhnicheskoi fiziki*. 2002, v. 72, iss. 10, p. 53-57 (in Russian).
13. V.O. Bomko, O.F. Dyachenko, O.M. Yegorov, et al. Development of investigations on the MILAC heavy ion linear accelerator // *Proc. of the LINAC08, Vancouver, Victoria, Canada*. 2008, p. 187-189.
14. R.A. Anokhin, B.V. Zaitsev, K.V. Pavlii, et al. Experimental complex for investigation of construction materials on the helium ions linear accelerator // *Problems of Atomic Science and Technology*. 2017, № 6, p. 167-171.
15. S.N. Dubniuk, R.A. Anokhin, A.F. Dyachenko, et al. Radiation complex on the basis of helium ions linac // *Problems of Atomic Science and Technology*. 2018, № 4, p. 46-51.
16. A.F. Dyachenko, R.A. Anokhin, S.N. Dubniuk, et al. The bunch formation and transport system to the target of the helium ions linac // *Problems of Atomic Science and Technology.* 2018, № 4, p. 52-55.
17. A.F. Dyachenko, S.N. Dubniuk, O.V. Manuilenko, et al. Improvement of helium ions beam formation and transport system // *Problems of Atomic Science and Technology.* 2021, № 6, p. 139-142.
18. R.A. Anokhin, S.N. Dubnyuk, A.F. Dyachenko, et al. Beam and target parameters measurement system on helium ions linear accelerator // *Problems of Atomic Science and Technology*. 2018, № 4, p. 30-35.
19. V.I. Butenko, S.N. Dubniuk, A.F. Dyachenko, et al. Constructional materials experimental researches on the helium ions linear accelerator // *Problems of Atomic Science and Technology*. 2021, № 4, p. 85-89.
20. V.I. Butenko, S.N. Dubniuk, A.F. Dyachenko, et al. Tribological characteristics of steel ceramics irradiated by helium ions pair // *Problems of Atomic Science and Technology*. 2021, № 5, p. 44-50.
21. I.M. Onishchenko, O.V. Manuilenko, B.V. Zajtsev, et al. Experimental research and work development on the helium ions linac // *Problems of Atomic Science and Technology*. 2021, № 6, p. 197-200.
22. V.I. Butenko, A. Cenian, O.F. Dyachenko, et al. TiO_2-2 radiating damages as a result of the irradiation helium ions with energies of 0.12 and 4 MeV on the linear accelerator // *Problems of Atomic Science and Technology*. 2023, № 4, p. 96-104.
23. K.V. Pavlii, S.N. Dubniuk, O.F. Dyachenko, et al. Electrophysical characteristics of TiO_2 samples irradiated with 0.12 MeV helium ions // *Problems of Atomic Science and Technology.* 2024, № 5, p. 103-110.
24. http://www.srim.org.
25. B. Widrow, J.R. Glover, J.M. McCool, et al. Adaptive noise cancelling: principles and applications // *Proc. IEEE*. 1975, v. 63, p. 1692-1716.

Article received 11.06.2025

ЕФЕКТ ДАЛЕКОДІЇ ПРИ ОПРОМІНЕННІ ЗРАЗКІВ TiO_2 НА ЛІНІЙНОМУ ПРИСКОРЮВАЧІ ІОНІВ ГЕЛІЮ

К.В. Павлій, В.І. Бутенко, О.Ф. Дьяченко, О.В. Мануйленко, Б.В. Зайцев

Наведено основні параметри опромінення зразків TiO_2 на лінійному прискорювачі іонів гелію та характеристики зразків, що опромінюються. Після опромінення TiO_2-2 іонами гелію з енергією 4 МеВ виявлено утворення флекінгу на лицьовій і тильній сторонах зразка, зменшення об'ємного електроопору та поверхневих електроопорів на лицьовій і тильній сторонах зразка, збільшення процентного вмісту титану й зменшення кисню на лицьовій і тильній сторонах опроміненого зразка, що свідчить про прояв ефекту далекодії. З урахуванням змінення профілю поверхні опромінених зразків розраховано первинні процеси, а саме: іонізація, утворення фононів і вакансій, сегрегація, пошкоджуваність та розпилення. Аналіз експериментальних даних показав, що модель, заснована на процесах збудження й поширення пружних хвиль, найбільш фізично правильно описує деякі ефекти далекодії.